

Imaging of interlayer coupling in van der Waals heterostructures using a bright-field optical microscope

Evgeny M. Alexeev^{1*}, Alessandro Catanzaro¹, Oleksandr V. Skrypka¹, and Alexander I. Tartakovskii¹

¹Department of Physics and Astronomy, University of Sheffield, Sheffield S3 7RH, UK

*e.alexeev@sheffield.ac.uk

ABSTRACT

By vertically stacking monolayer crystals of transition metal dichalcogenides (TMD) and other layered materials, a new type of heterostructures can be achieved, exhibiting novel opto-electronic properties. Such van der Waals heterostructures offer a platform for developing a new generation of atomically thin, transparent and flexible devices. The performance of these devices is primarily defined by the thickness of individual layers, as well as the coupling between them. The presence of organic residues between the atomic planes can significantly lower interlayer coupling efficiency, leading to reduced charge and energy transfer between the layers. In this paper, we demonstrate a method of monitoring interlayer coupling in TMD heterostructures through photoluminescence imaging using a bright-field optical microscope. We use the presented technique to track the changes of interlayer coupling and the emergence of interlayer excitons in TMD heterobilayers after annealing. Material and thickness sensitivity of photoluminescence imaging presented in this work makes it a powerful tool for characterisation of van der Waals heterostructures assembled by a wide variety of methods, using combinations of TMDs and other materials obtained through mechanical or chemical exfoliation and other fabrication techniques.

Introduction

Atomically thin materials offer a new paradigm for control of electronic excitations in the extreme two-dimensional (2D) limit in condensed matter. Recently this concept has been developed further with the creation of 2D heterostructures in which individual atomic layers are held together by van der Waals (vdW) interaction¹⁻⁴. The weak interlayer bonding loosens the lattice matching requirement, allowing a wide range of materials to be used in one device. Such vdW heterostructures combine unique properties of 2D materials with transparency and extreme flexibility, allowing a range of novel electronic and optoelectronic devices to be fabricated. Indeed, a wide variety of such devices has been demonstrated, including field-effect transistors^{3,5-9}, light emitting devices¹⁰⁻¹³, vertical tunneling transistors¹⁴⁻¹⁷ and photodetectors¹⁸⁻²⁴.

Stacking of atomically thin semiconductors such as transition metal dichalcogenides (TMDs) allows a new approach to band-gap engineering in structures with atomically sharp interfaces, in contrast with more traditional III-V semiconductors where the layer boundaries are blurred by the atomic interdiffusion. Type-II band alignment generally observed in TMD heterobilayers leads to efficient dissociation of optically excited intralayer excitons²⁵⁻²⁷, which is of potential value for photovoltaic and photodetector applications. In certain scenarios, charge separation also results in formation of interlayer excitons, in which electrons and holes are localised in different materials^{21,28-33}. Such excitons have binding energies comparable to those of their intralayer counterparts³⁴, however, they can have orders of magnitude longer lifetimes due to the spatial separation of the charges³¹. The radiative lifetime can be further increased by the introduction of hexagonal boron nitride spacer layers or rotational misalignment between the TMD layers, making interlayer excitons a promising platform for observation of high-temperature exciton condensation and superfluidity³⁵. The long lifetimes in conjunction with valley-dependent optical selection rules in individual TMD monolayers have made interlayer excitons promising for valley index manipulation and valleytronic applications³⁶: long-lived (40 ns) valley polarisation has recently been demonstrated for interlayer excitons in MoSe₂/WSe₂ heterostructures using circularly-polarised optical excitation³⁷.

While recent advantages in growth techniques have allowed lateral³⁸⁻⁴⁴ and vertical^{32,45,46} vdW heterostructures to be manufactured using CVD growth, the majority of prototype devices used in research of electronic and optical properties are still created by mechanical stacking of exfoliated crystals. Along with the fast device prototyping, this method offers the ultimate control of twist angle and overlap between different layers. The transfer methods utilised for vdW heterostructure fabrication through mechanical stacking rely on the use of a polymer, such as polymethylmethacrylate (PMMA)^{47,48} or

polydimethylsiloxane (PDMS)⁴⁹, as transfer medium. This often results in the presence of organic residues on crystal surfaces that can prevent efficient electronic and even mechanical coupling between adjacent layers. Thermal annealing in vacuum or inert atmosphere is often used to improve interlayer coupling in vdW heterostructures^{26,28,46,50–52}. Though such thermal treatment can significantly improve the coupling, the efficiency of this method strongly depends on the fabrication procedure used to build a given heterostructure and the annealing conditions themselves.

In this paper, we present a method for monitoring the interlayer coupling in vdW heterostructures using a bright-field optical microscope. We show that a bright photoluminescence (PL) image of the whole monolayer area of a mechanically exfoliated TMD crystal can be obtained using a standard microscope equipped with a white light source and a set of optical edge filters. The presented techniques can be utilised for rapid identification of TMD mono- and even few-layers on various substrates, including PMMA and PDMS commonly used for vdW heterostructure fabrication. We show that, by using appropriate bandpass filters, selective imaging of individual materials within a van der Waals heterostructure can be achieved. We further utilise the sensitivity of the optical properties of 2D TMD crystals to surrounding environment to monitor changes of interlayer coupling following annealing of the heterostructure. The microscope PL images unambiguously reveal that, while as-fabricated TMD heterobilayers act as a set of independent monolayers, significant improvement of interlayer coupling can be clearly observed after the thermal treatment. While TMD heterostructures with random layer orientation show significant PL quenching due to intralayer exciton dissociation, bright interlayer emission can be seen in heterobilayers with aligned principal crystal axes. The sensitivity of the TMD emission to the individual layer thickness and coupling between different layers makes microscope PL imaging a useful tool for vdW heterostructure characterisation with wide ranging applications.

Results

Experimental procedure

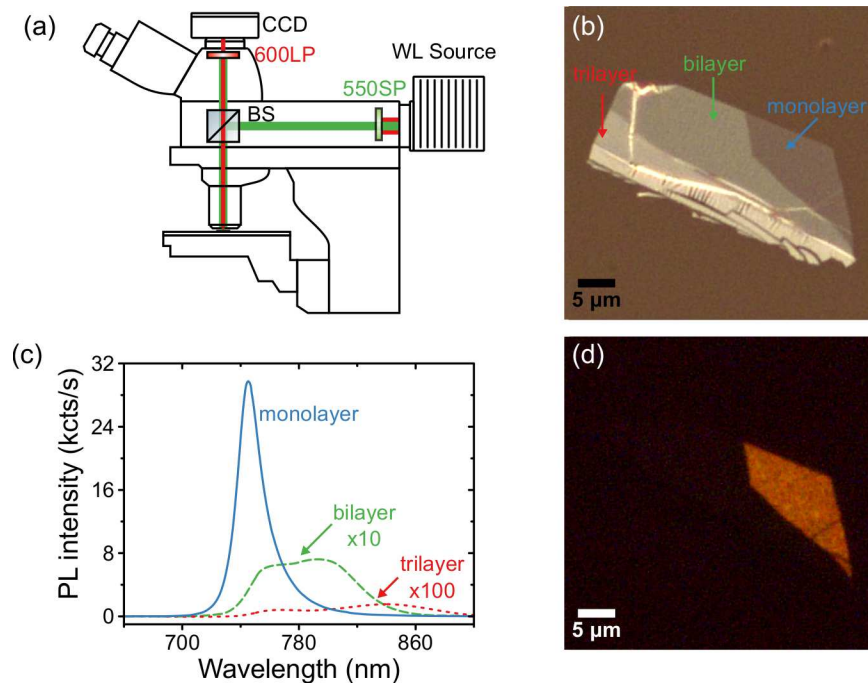


Figure 1. PL imaging of TMD monolayers using a bright-field optical microscope. (a) Schematic representation of the PL imaging set up. (b) Bright-field image of a mechanically exfoliated WSe₂ crystal on a PDMS substrate (c) PL spectra recorded in monolayer (solid blue), bilayer (dashed green) and trilayer (dotted red) regions of the sample (d) PL image of same sample acquired with 1 s acquisition time and 9.6x analog gain on the camera.

PL imaging of 2D TMD crystals was achieved using a commercial bright-field microscope (LV150N, Nikon). The schematic of the experimental setup is presented in Figure 1 (a). A 550 nm short-pass filter (FESH0550, Thorlabs) was used to block near-infrared emission from the white light source. PL signal produced by the sample was isolated using 600 nm long-pass filter (FELH0600, Thorlabs). The short-pass (long-pass) filters were installed into polariser (analyser) slots of the illuminator (LV-UEPI-N, Nikon), allowing quick switching between PL and bright-field imaging modes.

The PL images of the samples were acquired using a colour microscope camera (DS-Vi1, Nikon). While silicon CCD and CMOS sensors have their peak sensitivity at 800 nm, they can detect light with wavelength up to 1.1 μm . Most of the colour cameras, however, have a built-in hot mirror that limits their sensitivity to the visible spectrum. In order to enable the detection of near-infrared emission, this mirror has to be removed.

Figure 1 (b) shows a bright-field image of a WSe_2 flake exfoliated onto a PDMS substrate. The most translucent area in the top right corner of the flake corresponds to the monolayer region. The PL image of the same sample acquired using the experimental set up is shown in Figure 1 (d). Even with 1 second acquisition time, the monolayer region is clearly visible in the image due to bright PL emitted by the flake. The PL emission from the bilayer region is two orders of magnitude weaker and requires much longer acquisition times to be detected.

PL imaging offers a convenient method of characterising spatial variation of the emission intensity in TMD monolayers. Figure 1 (d) shows random variation of PL intensity across the monolayer region that can be caused by non-uniform doping, mechanical strain or presence of structural defects in the flake. The dark lines in the bottom right corner correspond to folds in the sample that can also be seen in the bright-field image (Fig. 1 (b)).

The thickness dependence of the PL intensity reflects the changes of the WSe_2 band structure with increasing numbers of layers⁵³. While monolayer WSe_2 is a direct bandgap semiconductor, the bandgap becomes indirect for bilayers, leading to a strong quenching of the PL. Figure 1 (c) compares PL spectra recorded in different regions of the flake using a separate micro-PL set up (see Methods for details). The monolayer region shows bright PL with emission peak centred at 745 nm (solid blue line). The direct-to-indirect bandgap transition in bilayer WSe_2 leads to a shift of the emission maximum to lower energies, as well as two orders of magnitude reduction of the emission intensity (dashed green line). Further increase of thickness leads to almost complete disappearance of the PL signal (dotted red line).

Photoluminescence imaging of monolayer transition metal dichalcogenides

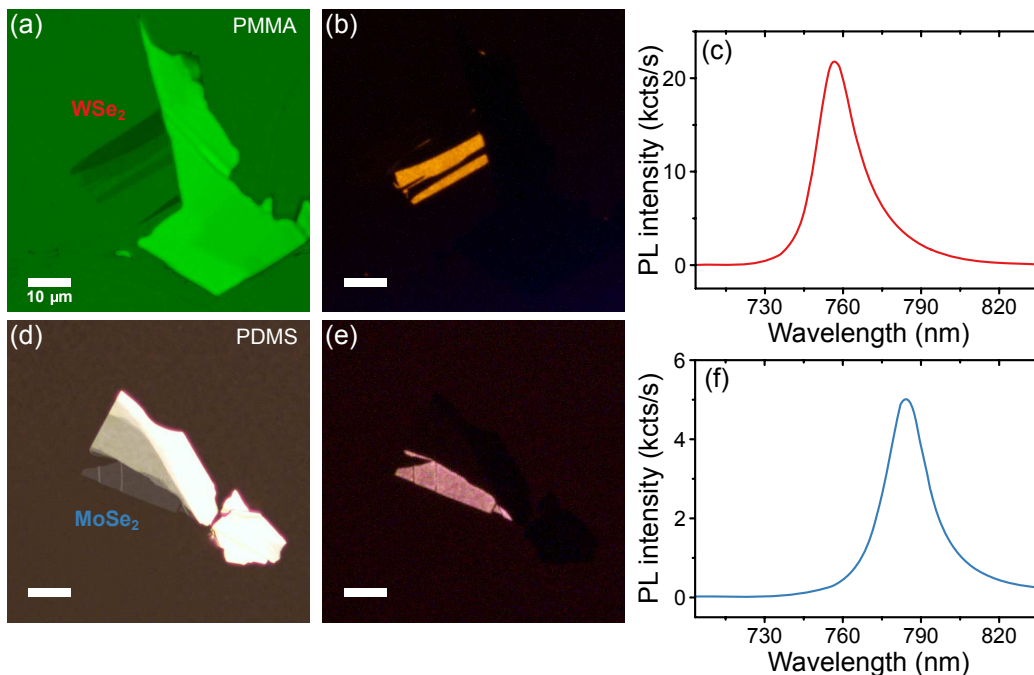


Figure 2. Optical identification of TMD monolayers on various substrates. (a) Bright-field image of a WSe_2 flake exfoliated onto PMMA-coated Si/SiO_2 substrate under green illumination. (b) PL image of the sample acquired using bright-field microscope. (c) PL spectrum recorded in the monolayer region of the sample using a micro-PL setup. (d) and (e) Bright-field and PL images of a MoSe_2 flake on a PDMS membrane. (f) PL spectrum of the single layer region.

The abrupt change of the emission intensity with increasing numbers of layers allows PL imaging to be used for rapid monolayer identification. Unlike other methods, such as optical contrast measurements⁵⁴, it relies on the change of the band structure and therefore is independent of the type of the substrate used. Figure 2 compares bright-field images of MoSe_2 and WSe_2 flakes exfoliated onto PMMA and PDMS membrane respectively; green illumination was used for imaging of the sample on the PMMA membrane in order to make the monolayer region visible⁵⁵. TMD flakes have very different appearances on

these two substrates, with few-layer areas showing negative (positive) optical contrast on PMMA (PDMS). Nevertheless, single layer regions of both samples can be easily identified in PL images (Fig. 2 (b) and (e)).

Different colours of MoSe₂ and WSe₂ in PL images reflect the difference between their emission spectra. Figure 2 (c) and (f) plots room-temperature PL spectra for the monolayer regions of both flakes recorded using the micro-PL set up. For MoSe₂, PL emission arising from exciton recombination is centred at 790 nm while for WSe₂ the exciton PL peaks at 750 nm. Colour imaging in digital cameras is achieved through the use of colour filter arrays, such as Bayer filter mosaic. The false colour in PL images is the result of the difference in the near-infrared transmission efficiency of these filters.

Photoluminescence imaging of van der Waals heterostructures

The material sensitivity of the PL imaging using a microscope makes it very useful for vdW heterostructure characterisation. Figure 3 show an optical image of MoSe₂/WSe₂ heterostructure assembled on Si/SiO₂ substrate using viscoelastic stamping method employing PDMS stamps⁴⁹. While both TMD crystals have similar appearances in the bright-field microscope image, the PL emission of their monolayer regions has noticeably different colours, allowing the two materials to be easily distinguished. Furthermore, selective imaging of different materials within the heterostructure can be achieved by replacing the long-pass filter in the detection path with an appropriate band-pass filter.

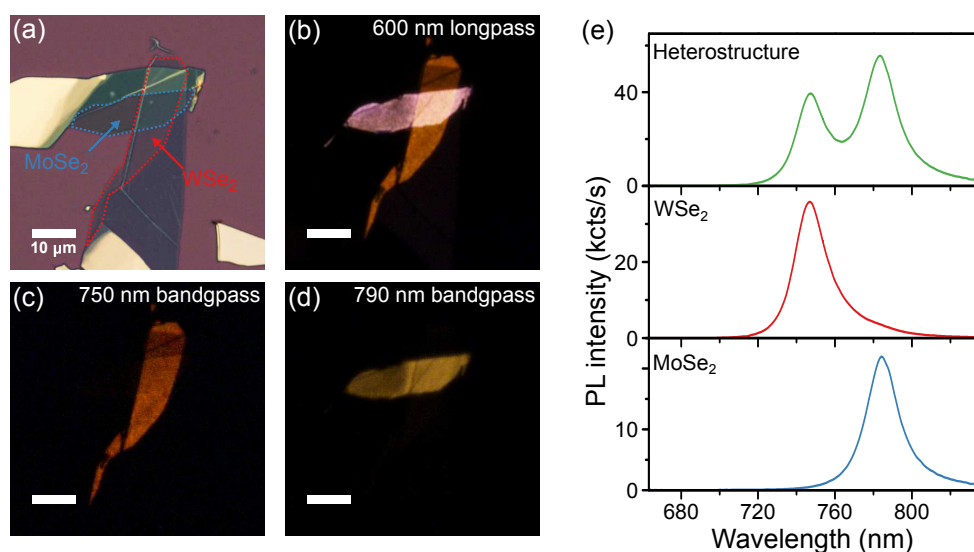


Figure 3. Selective imaging of different materials in a vdW heterostructure. (a) Bright-field image of a MoSe₂/WSe₂ heterostructure assembled on a Si/SiO₂ substrate by viscoelastic stamping. (b) PL image of the sample showing emission from the monolayer regions of both materials. (c) and (d) PL images of individual materials acquired using 750 nm (c) and 790 nm (d) bandpass filters for detection. (e) PL spectra acquired in the heterostructure (**top**), isolated WSe₂ (**middle**) and MoSe₂ (**bottom**) regions.

Figure 3 (c) and (d) shows PL images recorded using the bandpass filters with the transmission region centred at the emission wavelength of the corresponding material (750 nm (c) and 790 nm (d), for MoSe₂ and WSe₂ respectively). As the signal intensity was lowered by the use of a narrow-band filter, 10 s acquisition time was used for both images. Although emission maxima at room temperature for MoSe₂ and WSe₂ are positioned close to each other, the images demonstrate perfect selectivity, showing only the monolayer region of the chosen material. Figure 3 (e) plots PL spectra recorded in isolated MoSe₂ (bottom) and WSe₂ (middle) areas, as well as in the overlap region (top). As it is evident from both PL images and spectra, the emission of the heterostructure consists of the sum of MoSe₂ and WSe₂ emission, indicating a weak coupling between two layers.

The heterostructure formed by the MoSe₂ and WSe₂ monolayers has type-II band alignment that facilitates ultrafast charge separation between the two layers^{31,37}. For heterobilayers with a clean interlayer interface, this charge transfer acts as a dominant relaxation channel, significantly quenching intralayer excitonic PL. The largely unperturbed intralayer emission in the heterostructure region indicates that the interlayer coupling is suppressed by the polymer residues trapped between the two layers^{28,46}.

Imaging of interlayer coupling in van der Waals heterostructures

Thermal annealing in vacuum or inert atmosphere is commonly used to remove organic residues from the surface of 2D crystals^{26,28,46,50-52} and can also be utilised to improve interlayer coupling in an existing heterostructure. Figure 4 compares bright-field microscope images of the sample before (a) and after (d) annealing in high vacuum at 120° C for 2 hours. While a part of the isolated MoSe₂ monolayer was damaged during the thermal treatment, both isolated WSe₂ and heterostructure regions remain mostly intact.

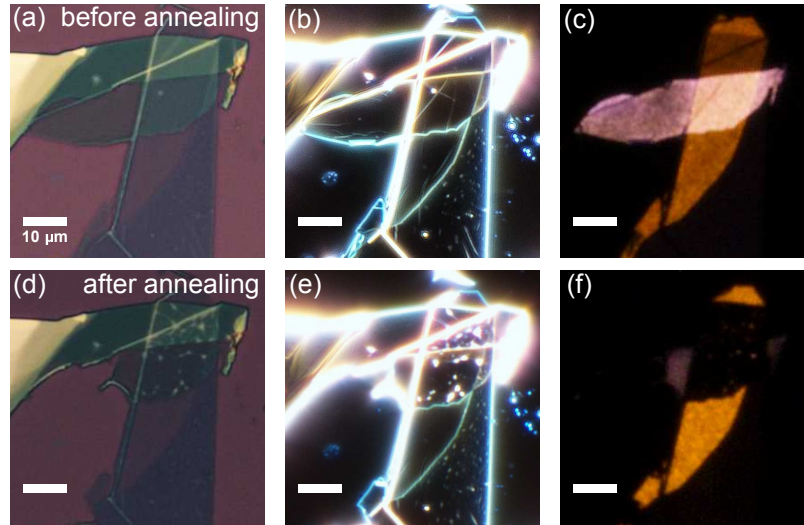


Figure 4. Monitoring the changes of interlayer coupling after thermal annealing. (a), (b) and (c) Bright-field, dark-field and PL images of a MoSe₂/WSe₂ heterostructure on a Si/SiO₂ substrate. (d), (e) and (f) Bright-field, dark-field and PL images of the same structure after annealing at 120° C in high vacuum for 2 hours.

Although the thermal treatment could not completely remove the organic residues trapped between the layers, it has caused their aggregation into small contamination pockets that can be clearly seen in both bright- and dark-field images (Fig. 4 (d) and (e)). Note that this process was not caused by thermal migration of residue particles, but is a result of strong attraction between two layers⁵⁶. Comparing the dark-field images acquired before and after annealing (Fig. 4 (b) and (e), respectively), it is apparent that the contamination pockets have formed only in the areas where the two crystals overlap. Moreover, we have not observed any residue aggregation in the heterostructures where the bottom crystal was annealed prior to the deposition of the top flake. The formation of contamination pockets after annealing is similar to the self-cleansing observed in vdW heterostructures^{4,57} and results in atomically clean interfaces in the contamination-free regions.

The effects of the thermal treatment on emission intensity can be clearly seen in the PL image of the sample taken after annealing. While the structural damage induced in the MoSe₂ have led to a reduction of its PL strength, substantial increase of the emission intensity due to removal of surface residues has occurred in the WSe₂ monolayer^{52,58}. The strongest change of the PL intensity can be seen in the overlap region, where both MoSe₂ and WSe₂ emission has almost completely disappeared after annealing. The reduction of the PL intensity in the heterobilayer region is a result of improved interlayer coupling. Type II band alignment in TMD heterobilayers leads to ultrafast interlayer charge separation that acts as the dominant relaxation channel, leading to almost complete quenching of the intralayer excitonic emission^{21,25-28,51,59-62}. The WSe₂ emission intensity is significantly reduced in all areas covered by MoSe₂, however, bright PL can still be observed in the parts of the heterostructure around the contamination pockets, where two layers remain uncoupled. Such pockets can also be clearly seen in the dark-field microscope image (Fig. 4 (e)).

The interlayer charge separation in TMD heterobilayers can lead to the formation of interlayer excitons formed by electrons and holes localised in different materials. The lack of any observable emission in the overlap region in Fig. 4 (f) is a result of the combination of the suppression of the interlayer exciton emission in MoSe₂/WSe₂ at elevated temperature and low efficiency of the CCD at the wavelength above 900 nm where the PL of the interlayer exciton is expected. A further important consideration is that the momentum-space alignment of $\pm K$ valleys in TMD heterobilayers depends of the relative layer orientation in the real space. In the presented structure, the crystal axes in the monolayers are not aligned, which leads to spatially- and momentum-space-indirect optical transitions only, which have negligible probability.

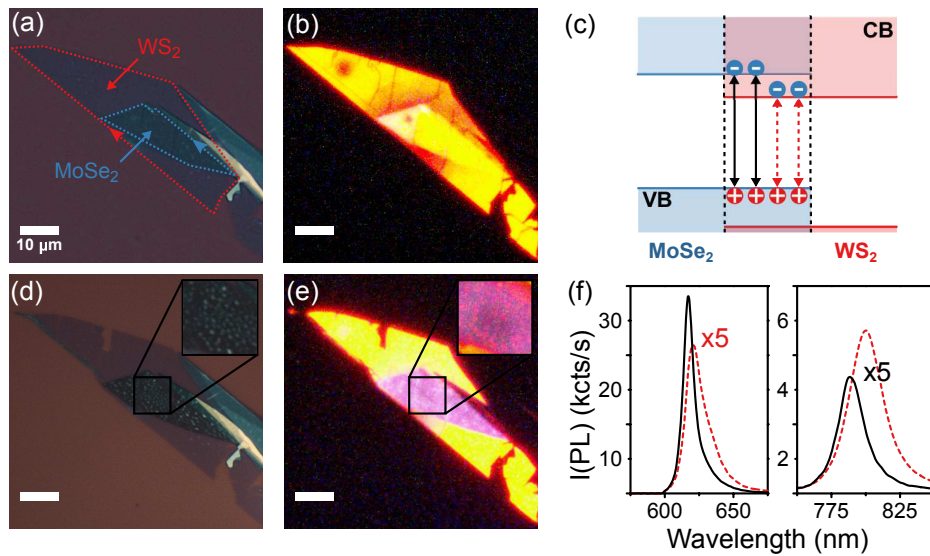


Figure 5. Emergence of interlayer emission after annealing. (a) and (b) Bright-field and PL images of a MoSe₂/WS₂ heterostructure on a Si/SiO₂ substrate. The crystal edges used for alignment are marked with arrows. (c) Band alignment of a MoSe₂/WS₂ heterostructure indicating intralayer (**solid black**) and interlayer (**dashed red**) optical transitions. (d) and (e) Bright-field and PL images of the sample after annealing. (f) PL spectra of the heterostructure before (**solid black**) and after (**dashed red**) annealing.

In order to investigate the effects of annealing on the formation of interlayer excitons in TMD heterobilayers, we have fabricated a set of heterostructures in which crystal axes of individual layers were aligned using their terminating edges as a guide⁶³. Figure 5 shows the bright-field (a) and PL (b) images of a MoSe₂/WS₂ heterostructure assembled on a Si/SiO₂ substrate using PDMS stamping; both images were taken before annealing. The PL emission in the overlap region consists mostly of WS₂ PL as at room temperature it is several orders of magnitude stronger than that of MoSe₂^{25,33}.

The improvement of the interlayer coupling leads to a significant change of the heterostructure emission that can be clearly seen in the PL image (Fig. 5 (e)). While isolated monolayer regions of WS₂ show an increase of the PL intensity due to removal of the polymer residues, the heterostructure region demonstrates a prominent change of emission colour, indicating a significant shift of its peak emission wavelength.

Figure 5 (f) compares the PL spectra of the heterostructure before (solid black) and after (dashed red) annealing. Prior to the thermal treatment, the WS₂ emission is two orders of magnitude stronger than that of MoSe₂. Unlike the isolated monolayer regions, WS₂ emission in the heterostructure is significantly quenched after annealing due to the efficient interlayer charge separation^{25,33}. The 3 nm red-shift of the WS₂ peak is caused by strain induced in the sample during annealing due to the difference in thermal expansion coefficient between the sample and the supporting substrate^{64–66}. The emergence of a strong peak at 800 nm following the annealing indicates the formation of interlayer excitons. The emission energy of these excitons is defined by conduction and valence band offsets between two materials (Fig. 5 (c)). Unlike MoSe₂/WS₂ heterobilayers, the near-degenerate conduction bands in MoSe₂/WS₂ heterostructure result in interlayer exciton states that lay just few tens of meV below the MoSe₂ exciton states³³. The regions of the heterostructure containing contamination pockets are visible as spots of a different colour in the PL image (Fig. 5 (e)). The PL in these areas mostly comes from WS₂, as the aggregated residues prevent efficient coupling between two materials, causing them to act as independent layers.

As most of the transfer methods result in organic residues at the crystal surfaces, sample annealing becomes an essential step in vdW heterostructure fabrication. However, in some cases it can also result in significant degradation of the sample quality. The PL imaging developed in this work offers a convenient method of characterisation of the effects of the thermal treatment on optical properties of heterostructures that does not require the use of a dedicated optical set up equipped with a spectrometer. The short acquisition times make it possible to investigate changes of the interlayer coupling in real time, allowing PL imaging to be used for in-situ monitoring of sample annealing. The ability to selectively image individual materials makes it a useful tool for TMD monolayer alignment in multilayer vdW heterostructures.

In summary, we have demonstrated that fast large area PL imaging of 2D TMD samples can be achieved using a bright-field optical microscope. The presented technique offers a convenient way of combining flake search and thickness identification in one experimental set up. We have shown that PL imaging can be utilised to monitor changes of interlayer coupling in TMD heterostructures caused by thermal annealing. Improvement of the coupling efficiency and formation of interlayer excitons in

TMD heterobilayers after thermal treatment can be clearly observed in the microscope PL images. As the presence of defects in TMDs leads to quenching of their PL, it is also possible to use the reported PL imaging method for quality control of monolayer semiconductor crystals.

Methods

Sample preparation

Monolayer and few-layer TMD crystals were mechanically exfoliated from bulk crystals (provided by HQ graphene) using wafer backgrinding tape (BT-150E-CM, Nitto). Van der Waals heterostructures were fabricated by exfoliating material onto a PDMS membrane (PF X4, Gel-Pak) followed by a transfer onto Si/SiO₂ using a viscoelastic stamping method.

Optical measurements

Spectrally resolved PL measurements were performed in a custom-built micro-PL set up. A diode-pumped solid state laser at 532 nm (ADL-66505TL, Roithner) was focused onto the sample using 50x objective lens (M Plan Apo 50X, Mitutoyo). The PL signal collected in the backwards direction was isolated using a 550 nm shortpass filter (FES0550, Thorlabs) and detected by spectrometer (SP-2-500i, Princeton Instruments) with nitrogen cooled CCD camera (PyLoN:100BR, Princeton Instruments). All spectrally resolved PL measurements were performed at room temperature and in ambient conditions.

References

1. Li, M. Y., Chen, C. H., Shi, Y. & Li, L. J. Heterostructures based on two-dimensional layered materials and their potential applications. *Materials Today* **19**, 322–335 (2015).
2. Geim, A. K. & Grigorieva, I. V. Van der Waals heterostructures. *Nature* **499**, 419–425 (2014).
3. Liu, Y. *et al.* Van der Waals heterostructures and devices. *Nature Reviews Materials* 16042 (2016).
4. Novoselov, K. S., Mishchenko, A., Carvalho, A., Neto, A. H. C. & Road, O. 2D materials and van der Waals heterostructures. *Science* **353**, aac9439 (2016).
5. Roy, T. *et al.* Field-effect transistors built from all two-dimensional material components. *ACS Nano* **8**, 6259–6264 (2014).
6. Das, S., Gulotty, R., Sumant, A. V. & Roelofs, A. All two-dimensional, flexible, transparent, and thinnest thin film transistor. *Nano Letters* **14**, 2861–2866 (2014).
7. Lee, G.-h. *et al.* Highly Stable, Dual-Gated MoS₂ Transistors Encapsulated by Hexagonal Boron Nitride with Gate-Controllable Contact, Resistane and Threshold Voltage. *ACS Nano* **9**, 7019–7026 (2015).
8. Liu, Y. *et al.* Toward barrier free contact to molybdenum disulfide using graphene electrodes. *Nano Letters* **15**, 3030–3034 (2015).
9. Cui, X. *et al.* Multi-terminal transport measurements of MoS₂ using a van der Waals heterostructure device platform. *Nature Nanotechnology* **10**, 534–540 (2015).
10. Ross, J. S. *et al.* Electrically tunable excitonic light-emitting diodes based on monolayer WSe₂ p-n junctions. *Nature nanotechnology* **9**, 268–72 (2014).
11. Cheng, R. *et al.* Electroluminescence and photocurrent generation from atomically sharp WSe₂/MoS₂ heterojunction p-n diodes. *Nano Letters* **14**, 5590–5597 (2014).
12. Withers, F. *et al.* WSe₂ Light-Emitting Tunneling Transistors with Enhanced Brightness at Room Temperature. *Nano Letters* **15**, 8223–8228 (2015).
13. Withers, F. *et al.* Light-emitting diodes by band-structure engineering in van der Waals heterostructures. *Nature Materials* **14**, 301–306 (2015).
14. Britnell, L. *et al.* Field-Effect Tunneling Transistor Based on Vertical Graphene Heterostructures. *Science* **335**, 947–950 (2012).
15. Britnell, L. *et al.* Resonant tunnelling and negative differential conductance in graphene transistors. *Nature communications* **4**, 1794 (2013).
16. Lin, Y.-C. *et al.* Atomically thin resonant tunnel diodes built from synthetic van der Waals heterostructures. *Nature communications* **6**, 7311 (2015).
17. Roy, T. *et al.* Dual-Gated MoS₂/WSe₂ van der Waals Tunnel Diodes and Transistors. *ACS Nano* **9**, 2071–2079 (2015).

18. Buscema, M. *et al.* Photocurrent generation with two-dimensional van der Waals semiconductors. *Chem Soc Rev* **44**, 3691–3718 (2015).
19. Buscema, M., Groenendijk, D. J., Steele, G. a., van der Zant, H. S. J. & Castellanos-Gomez, A. Photovoltaic effect in few-layer black phosphorus PN junctions defined by local electrostatic gating. *Nature communications* **5**, 4651 (2014).
20. Furchi, M. M. *et al.* Photovoltaic effect in an electrically tunable Van der Waals heterojunction. *Nano Letters* **14**, 4785–4791 (2014).
21. Lee, C.-H. *et al.* Atomically thin p–n junctions with van der Waals heterointerfaces. *Nature Nanotechnology* **9**, 676–681 (2014).
22. Lou, J., Xu, X. & Ye, P. D. Black Phosphorus À Monolayer MoS₂ Diode. *ACS Nano* **8**, 8292–8299 (2014).
23. Massicotte, M. *et al.* Picosecond photoresponse in van der Waals heterostructures. *Nature nanotechnology* **11**, 1–6 (2015).
24. Yu, W. J. *et al.* Unusually efficient photocurrent extraction in monolayer van der Waals heterostructure by tunnelling through discretized barriers. *Nature Communications* **7**, 13278 (2016).
25. Kozawa, D. *et al.* Evidence for interlayer energy transfer in MoSe₂/WS₂ heterostructures. *Nano Letters* **16**, 4087–4093 (2016).
26. Zhang, K. *et al.* Interlayer Transition and Infrared Photodetection in Atomically Thin Type-II MoTe₂/MoS₂ van der Waals Heterostructures. *ACS Nano* **10**, 3852–3858 (2016).
27. Ceballos, F., Bellus, M. Z., Chiu, H.-Y. & Zhao, H. Ultrafast Charge Separation and Indirect Exciton Formation in a MoS₂–MoSe₂ van der Waals Heterostructure. *ACS Nano* **8**, 12717–12724 (2014).
28. Tongay, S. *et al.* Tuning interlayer coupling in large-area heterostructures with CVD-grown MoS₂ and WS₂ monolayers. *Nano Letters* **14**, 3185–3190 (2014).
29. Fang, H. *et al.* Strong interlayer coupling in van der Waals heterostructures built from single-layer chalcogenides. *Proceedings of the National Academy of Sciences of the United States of America* **111**, 6198–202 (2014).
30. Lui, C. H. *et al.* Observation of interlayer phonon modes in van der Waals heterostructures. *Physical Review B - Condensed Matter and Materials Physics* **91**, 1–7 (2015).
31. Rivera, P. *et al.* Observation of long-lived interlayer excitons in monolayer MoSe₂-WSe₂ heterostructures. *Nature communications* **6**, 6242 (2015).
32. Heo, H. *et al.* Interlayer orientation-dependent light absorption and emission in monolayer semiconductor stacks. *Nature Communications* **6**, 7372 (2015).
33. Ceballos, F., Bellus, M. Z., Chiu, H.-Y. & Zhao, H. Probing charge transfer excitons in a MoSe₂–WS₂ van der Waals heterostructure. *Nanoscale* **7**, 17523–17528 (2015).
34. Wilson, N. R. *et al.* Band parameters and hybridization in 2D semiconductor heterostructures from photoemission spectroscopy. *Arxiv* 10 (2016).
35. Fogler, M. M., Butov, L. V. & Novoselov, K. S. High-temperature superfluidity with indirect excitons in van der Waals heterostructures. *Nature communications* **5**, 4555 (2014).
36. Schaibley, J. R. *et al.* Valleytronics in 2D materials. *Nature Reviews Materials* **1**, 16055 (2016).
37. Rivera, P. *et al.* Valley-Polarized Exciton Dynamics in a 2D Semiconductor Heterostructure. *Science* **351**, 688 (2016).
38. Huang, C. *et al.* Lateral heterojunctions within monolayer MoSe₂–WSe₂ semiconductors. *Nature Materials* **13**, 1–6 (2014).
39. Duan, X. *et al.* Lateral epitaxial growth of two-dimensional layered semiconductor heterojunctions. *Nat Nanotechnol* **9**, 1024–1030 (2014).
40. Gong, Y. *et al.* Two-Step Growth of Two-Dimensional WSe₂/MoSe₂ Heterostructures. *Nano Letters* **15**, 6135–6141 (2015).
41. Yoshida, S. *et al.* Microscopic basis for the band engineering of Mo(1-x)W(x)S₂-based heterojunction. *Scientific Reports* **5**, 14808 (2015).
42. Li, H. *et al.* Lateral growth of composition graded atomic layer MoS₂(1-x)Se_{2x} nanosheets. *Journal of the American Chemical Society* **137**, 5284–5287 (2015).
43. Li, M.-Y. *et al.* Epitaxial growth of a monolayer WSe₂-MoS₂ lateral p-n junction with an atomically sharp interface. *Science* **349**, 524–8 (2015).

44. Pant, A. *et al.* Fundamentals of lateral and vertical heterojunctions of atomically thin materials. *Nanoscale* **8**, 3870–3887 (2016).
45. Gong, Y. *et al.* Vertical and in-plane heterostructures from WS₂/MoS₂ monolayers. *Nat Mater* **13**, 1135–1142 (2014).
46. Yu, Y. *et al.* Equally Efficient Interlayer Exciton Relaxation and Improved Absorption in Epitaxial and Nonepitaxial MoS₂/WS₂ Heterostructures. *Nano Letters* **15**, 486–491 (2015).
47. Dean, C. R. *et al.* Boron nitride substrates for high-quality graphene electronics. *Nature nanotechnology* **5**, 722–726 (2010).
48. Uwanno, T., Hattori, Y., Taniguchi, T., Watanabe, K. & Nagashio, K. Fully dry PMMA transfer of graphene on h-BN using a heating/cooling system. *2D Materials* **2**, 041002 (2015).
49. Castellanos-Gomez, A. *et al.* Deterministic transfer of two-dimensional materials by all-dry viscoelastic stamping. *2D Materials* **1**, 011002 (2014).
50. Chiu, M. H. *et al.* Spectroscopic signatures for interlayer coupling in MoS₂-WSe₂ van der waals stacking. *ACS Nano* **8**, 9649–9656 (2014).
51. Hong, X. *et al.* Ultrafast charge transfer in atomically thin MoS₂/WS₂ heterostructures. *Nature Nanotechnology* **9**, 1–5 (2014).
52. Wang, K. *et al.* Interlayer Coupling in Twisted WSe₂/WS₂ Bilayer Heterostructures Revealed by Optical Spectroscopy. *ACS Nano* acsnano.6b01486 (2016).
53. Tonndorf, P. *et al.* Photoluminescence emission and Raman response of monolayer MoS₂, MoSe₂, and WSe₂. *Optics Express* **21**, 4908 (2013).
54. Casiraghi, C. *et al.* Rayleigh imaging of graphene and graphene layers. *Nano Letters* **7**, 2711–2717 (2007).
55. Blake, P. *et al.* Making graphene visible. *Applied Physics Letters* **91** (2007).
56. Vasu, K. S. *et al.* Van der Waals pressure and its effect on trapped interlayer molecules. *Nature Communications* **7**, 1–24 (2016).
57. Kretinin, A. V. *et al.* Electronic Properties of Graphene Encapsulated with Different Two-Dimensional Atomic Crystals. *Nano Letters* **14**, 3270–3276 (2014).
58. Su, L., Yu, Y., Cao, L. & Zhang, Y. In-Situ Monitoring of Thermal Annealing Induced Evolution in Film Morphology and Film-Substrate Bonding in a Monolayer MoS₂ Film. *ArXiv e-prints* (2016).
59. Zhu, X. *et al.* Charge Transfer Excitons at van der Waals Interfaces. *Journal of the American Chemical Society* **137**, 8313–8320 (2015).
60. He, J. *et al.* Electron transfer and coupling in graphene-tungsten disulfide van der Waals heterostructures. *Nature communications* **5**, 5622 (2014).
61. Chen, H. *et al.* Ultrafast formation of interlayer hot excitons in atomically thin MoS₂/WS₂ heterostructures. *Nature Communications* **7**, 12512 (2016).
62. Yu, H., Wang, Y., Tong, Q., Xu, X. & Yao, W. Anomalous Light Cones and Valley Optical Selection Rules of Interlayer Excitons in Twisted Heterobilayers. *Physical Review Letters* **115**, 1–5 (2015).
63. Neubeck, S. *et al.* Direct determination of the crystallographic orientation of graphene edges by atomic resolution imaging. *Applied Physics Letters* **97**, 2010–2012 (2010).
64. Ryu, S. *et al.* Atmospheric oxygen binding and hole doping in deformed graphene on a SiO₂ substrate. *Nano Letters* **10**, 4944–4951 (2010).
65. Lee, J. E., Ahn, G., Shim, J., Lee, Y. S. & Ryu, S. Optical separation of mechanical strain from charge doping in graphene. *Nature Communications* **3**, 1024 (2012).
66. McCreary, K. M. *et al.* The Effect of Preparation Conditions on Raman and Photoluminescence of Monolayer WS₂. *Scientific Reports* **6**, 35154 (2016).

Acknowledgements

We thank the financial support of the EPSRC Programme Grant EP/J007544/1 and grant EP/M012727/1, Graphene Flagship under grant agreement 696656, and ITN Spin-NANO under grant agreement 676108.

Author contributions statement

E.M.A. and A.I.T. conceived the experiment. E.M.A. and A.C. fabricated samples. E.M.A and O.V.S carried out all optical measurements and analysed the results. E.M.A. wrote the manuscript with contribution from A.I.T. All authors reviewed the manuscript.